Analytical and Bioanalytical Chemistry (2020) 412:4067–4075
https://doi.org/10.1007/s00216-020-02630-8

RESEARCH PAPER

Electrochemiluminescence reaction pathways in nanofluidic devices

Silvia Voci[1] · Hanan Al-Kutubi[2] · Liza Rassaei[3] · Klaus Mathwig[4] · Neso Sojic[1,5]

Received: 27 February 2020 / Revised: 25 March 2020 / Accepted: 30 March 2020 / Published online: 28 April 2020

Abstract

Nanofluidic electrochemical devices confine the volume of chemical reactions to femtoliters. When employed for light generation by electrochemiluminescence (ECL), nanofluidic confinement yields enhanced intensity and robust luminescence. Here, we investigate different ECL pathways, namely coreactant and annihilation ECL in a single nanochannel and compare light emission profiles. By high-resolution imaging of electrode areas, we show that different reaction schemes produce very different emission profiles in the unique confined geometry of a nanochannel. The confrontation of experimental results with finite element simulation gives further insight into the exact reaction ECL pathways. We find that emission strongly depends on depletion, geometric exclusion, and recycling of reactants in the nanofluidic device.

Keywords Electrochemiluminescence · Electroanalytical methods · Nanofluidic device · Fluorescence/luminescence

Introduction

Electrochemiluminescence (ECL) is a controllable form of chemiluminescence where light emission results from an initial electron-transfer reaction occurring at an electrode surface [1–5]. It is a powerful analytical method with remarkable performances due to its dual intrinsic nature, which is based on the combination of electrochemistry and photophysics. ECL provides many advantages for analytical applications: time, duration, and position of the ECL-emitting region can be manipulated electrochemically [6–8]. In addition, it allows the simultaneous measurement of two experimental parameters (i.e., Faradaic current and light intensity) as a function of the applied potential, like fluorescence-based spectroelectrochemistry techniques [9–11]. Therefore, ECL offers a great selectivity and control over the light-emitting reactions. The most extensively investigated electrochemiluminophore is tris(2,2′-bipyridyl)ruthenium(II), $[Ru(bpy)_3]^{2+}$, which can be considered as an ECL standard. Using this compound, ECL emission can be triggered using several different reaction pathways (see Fig. 1). It can be initiated through the annihilation mechanism (reactions 1–4) between its oxidized and reduced forms (i.e., $[Ru(bpy)_3]^{3+}$ and $[Ru(bpy)_3]^{+}$, respectively). This is a very simple mechanistic pathway since it requires only the solvent, the supporting electrolyte and the electrochemiluminophore [7, 12–14]. Both species are generated in the vicinity of the electrode surface either by alternate pulsing of the electrode potential or by using a double-electrode configuration, where oxidation and reduction occur on each electrode (reactions 1–2). The homogeneous high-energy electron-transfer annihilation reaction between $[Ru(bpy)_3]^{3+}$ and $[Ru(bpy)_3]^{+}$ (reaction 3) populates the excited state. Finally, it decays to the ground state by emitting light (reaction 4).

$$\left[Ru(bpy)_3\right]^{2+} + e^- \rightarrow \left[Ru(bpy)_3\right]^{+} \quad (1)$$

Silvia Voci and Hanan Al-Kutubi contributed equally to this work.

Electronic supplementary material The online version of this article (https://doi.org/10.1007/s00216-020-02630-8) contains supplementary material, which is available to authorized users.

✉ Klaus Mathwig
k.h.mathwig@rug.nl

✉ Neso Sojic
Neso.Sojic@enscbp.fr

Liza Rassaei
rassaei.liza@gmail.com

[1] Bordeaux INP, Univ. Bordeaux, CNRS, ISM, UMR 5255, Site ENSCBP, 16, Avenue Pey-Berland, 33607 Pessac, France

[2] Department of Radiation Science and Technology, Delft University of Technology, Mekelweg 15, 2629 JB Delft, The Netherlands

[3] Rotterdam, The Netherlands

[4] Groningen Research Institute of Pharmacy, Pharmaceutical Analysis, University of Groningen, P.O. Box 196, 9700 AG Groningen, The Netherlands

[5] Department of Chemistry, South Ural State University, Chelyabinsk, Russian Federation 454080

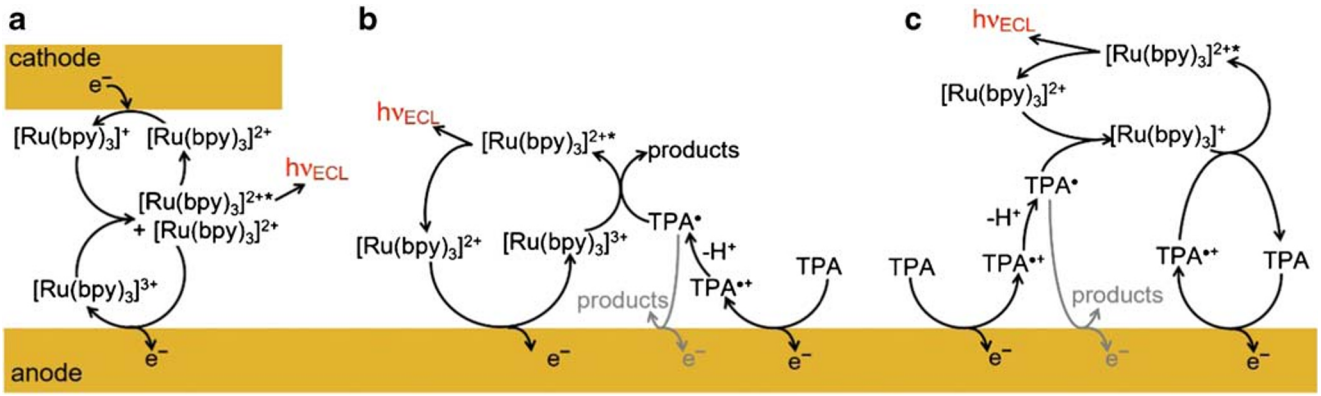

Fig. 1 Schematic of ECL reaction pathways. **a** Direct current annihilation pathway using exclusively $[Ru(bpy)_3]^{2+}$ luminophores (reactions 1–4). **b** Coreactant pathway with oxidation of $[Ru(bpy)_3]^{2+}$ and TPA coreactant at the electrode (reactions 5–9, 12). **c** Competing "revisited" coreactant route where only TPA is oxidized at the electrode (reactions 6, 7, 10, 11, and 12)

$$[Ru(bpy)_3]^{2+} - e^- \rightarrow [Ru(bpy)_3]^{3+} \quad (2)$$

$$[Ru(bpy)_3]^{+} + [Ru(bpy)_3]^{3+} \rightarrow [Ru(bpy)_3]^{2+} + [Ru(bpy)_3]^{2+*} \quad (3)$$

$$[Ru(bpy)_3]^{2+*} \rightarrow [Ru(bpy)_3]^{2+} + h\nu. \quad (4)$$

An alternative major pathway is based on the use of a coreactant species. A coreactant is a sacrificial species that is consumed irreversibly during the process. Its function is to generate highly oxidizing or reducing radicals that can react with the electrochemiluminophore to populate its excited state. Amine-based coreactants such as tri-n-propylamine (TPA), NADH or 2-(dibutylamino)ethanol (DBAE) follow the oxidative-reduction path [15]. For TPA, which is still the most widely used coreactant with the $[Ru(bpy)_3]^{2+}$ luminophore, several competitive mechanistic pathways have been proposed depending on the electrode materials, the pH value, the presence of surfactants, the applied potential, the immobilization of the luminophores in heterogeneous assays, etc. [16, 17]. In the present case, $[Ru(bpy)_3]^{2+}$ and TPA are first both oxidized at the electrode surface, generating $[Ru(bpy)_3]^{3+}$ and the cation radical $TPA^{\bullet+}$, respectively (reactions 5 and 6). Then, upon deprotonation (reaction 7), $TPA^{\bullet+}$ forms a strongly reducing radical $TPA^{\bullet}$ that reduces $[Ru(bpy)_3]^{3+}$ and generates $[Ru(bpy)_3]^{2+*}$ (reaction 8). $[Ru(bpy)_3]^{2+*}$ emits ECL light at a typical wavelength of 620 nm (reaction 9).

$$[Ru(bpy)_3]^{2+} - e^- \rightarrow [Ru(bpy)_3]^{3+} \quad (5)$$

$$TPA - e^- \rightarrow TPA^{\bullet+} \quad (6)$$

$$TPA^{\bullet+} \rightarrow TPA^{\bullet} + H^+ \quad (7)$$

$$[Ru(bpy)_3]^{3+} + TPA^{\bullet} \rightarrow [Ru(bpy)_3]^{2+*} + \text{products} \quad (8)$$

$$[Ru(bpy)_3]^{2+*} \rightarrow [Ru(bpy)_3]^{2+} + h\nu \quad (9)$$

The above reaction pathway is competing with the "revisited" coreactant reaction route [16]. In a solution containing both TPA and $[Ru(bpy)_3]^{2+}$, the electrochemiluminophore is not oxidized to $[Ru(bpy)_3]^{3+}$ at the electrode surface. Only the coreactant is oxidized directly at the electrode surface and deprotonates to form $TPA^{\bullet}$. Then, $TPA^{\bullet}$ reduces $[Ru(bpy)_3]^{2+}$ to $[Ru(bpy)_3]^{+}$, which is subsequently oxidized by $TPA^{\bullet+}$ to generate the light emitting state:

$$TPA^{\bullet} + [Ru(bpy)_3]^{2+} \rightarrow [Ru(bpy)_3]^{+} + \text{products} \quad (10)$$

$$TPA^{\bullet+} + [Ru(bpy)_3]^{+} \rightarrow TPA + [Ru(bpy)_3]^{2+*} \quad (11)$$

In both coreactant schemes, $TPA^{\bullet}$ radicals can also be oxidized at the electrode surface to form end-products:

$$TPA^{\bullet} \rightarrow e^- + \text{products} \quad (12)$$

All three reaction routes are shown in Fig. 1.

The third reaction route does not involve direct electron-transfer reactions of $[Ru(bpy)_3]^{2+}$ at the electrode surface; generation of the luminophore excited state and light emission takes place 1–2 μm further [16, 17]. Nonetheless, light emission is confined to an area in close vicinity (several hundreds of nm) of the electrode surface: the maximum emission distance from the electrode is limited by the lifetime τ of the radical $TPA^{\bullet+}$ of about 0.2 ms before deprotonation [16, 17] (i.e., to a distance <3 μm).

We have recently employed microfabricated nanofluidic electrochemical devices [18, 19] to generate and image ECL [20]. In such thin-layer-cell devices, chemical reactions are limited to a volume of about 10 femtoliters. The reaction compounds are geometrically confined by the walls of a nanochannel of several 10-μm length, which is connected to a reservoir via access holes (see Fig. 2). The channel floor and

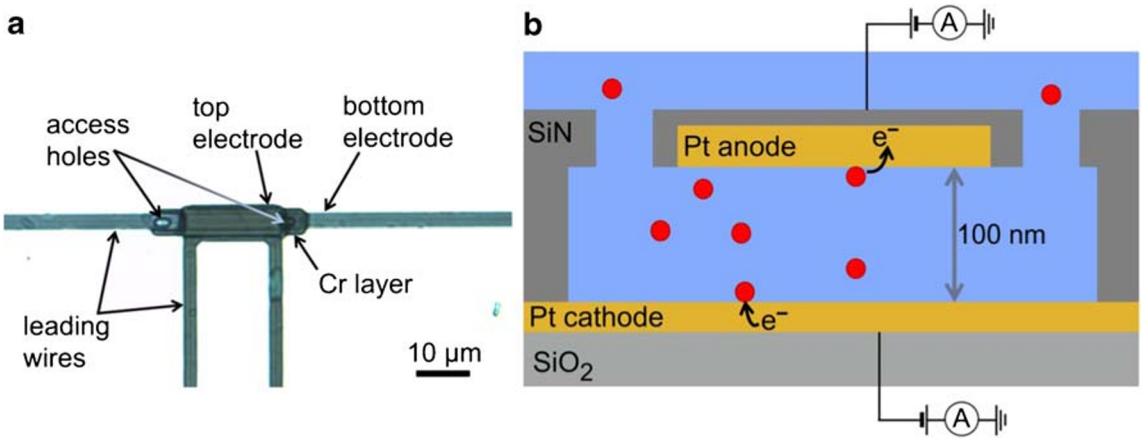

Fig. 2 **a** Top-view micrograph of a transparent nanofluidic device, before fully etching the Cr sacrificial layer forming the nanochannel volume. **b** Schematic cross section of a device. A nanochannel of 20-µm length is confined between two individually addressable Pt electrodes enclosed in a silicon nitride passivation layer. Access holes connect the nanochannel to a reservoir. Light emission is detected through a 20-nm-thin bottom electrode and a transparent borosilicate substrate

ceiling consist of Pt electrodes separated by a nanochannel height of only 100 nm. As nanoelectrochemical tools, nanofluidic devices enable the sensitive detection and manipulation of minute amounts of redox analytes [21–23]. When employing transparent devices for generating ECL using a $[Ru(bpy)_3]^{2+}$ annihilation reaction (see Fig. 1a), we observed very intense light emission due to the very short diffusional distance between both electrodes [20]: reduced $[Ru(bpy)_3]^{+}$ and oxidized $[Ru(bpy)_3]^{3+}$ combine and generate the light-emitting $[Ru(bpy)_3]^{2+*}$ state after only a microsecond diffusion time along a 50-nm distance to the center of the nanochannel.

Here, we explore and study different ECL reaction pathways in nanofluidic electrochemical devices. We observe distinct spatial emission intensity profiles for coreactant and annihilation routes (which are dictated by reaction rate and reactant lifetimes), demonstrate annihilation in the presence of TPA and estimate contribution of both competing coreactant pathways by finite element calculations.

Materials and methods

Device fabrication

The fabrication process has been described previously [20, 24]. Briefly, nanochannel devices consist of Si_3N_4/SiO_2 deposited on a transparent borosilicate substrate. They have a length of 20 µm, a width of 5 µm, and a height of 100 nm. 2 µm × 2 µm access holes at both ends of the nanochannel connect it to a fluidic reservoir. The entire ceiling of the nanochannel consist of the Pt top electrode. A 3-µm wide Pt bottom electrode is positioned on the nanochannel floor. Both electrodes overlap to form an active volume of 20 µm × 3 µm × 100 nm = 6 fL. The bottom electrode is 20 nm thin and, thus, semi-transparent, allowing imaging of light emission from the active volume using an inverted microscope objective. Devices were microfabricated by consecutive steps of photolithographical definition, deposition of metals and oxides, and plasma etching of access holes. The nanochannel volume is defined by a sacrificial Cr layer deposited by electron beam evaporation. This layer protects the Pt electrode surface and is removed before electrochemical experimentation using a selective wet-chemical etch. Pt electrodes were cleaned by sweeping the potential of both electrodes repeatedly between − 0.15 V and 1.2 V vs. Ag/AgCl in 500 mM sulfuric acid.

Chemicals

ECL experiments were conducted using a solution of HPLC-grade acetonitrile containing 10 mM tris(2,2′-bipyridine)ruthenium(II) hexafluorophosphate ($Ru(bpy)_3(PF_6)_2$) as electrochemiluminophore, 100 mM tri-n-propylamine (TPA) coreactant, and 100 mM tetrabutylammonium hexafluorophosphate ($TBAPF_6$) electrolyte. All compounds were purchased from Sigma-Aldrich. Selectipur chromium etchant, used to wet-etch the sacrificial Cr layer to release the nanochannel, was purchased from BASF.

Instrumentation

Top and bottom electrodes of a nanofluidic device were connected to a bipotentiostat (Autolab–PGSTAT30, used for all electrochemical measurements) via microstructured leading wires and needle probes. A fluidic reservoir in polydimethylsiloxane was placed on top of the device. A reference electrode was placed in this reservoir, either a Ag/AgCl/KCl (3 M) electrode in aqueous solvent, or a Ag wire for measurements

in acetonitrile (no dedicated counter electrode was used at low μA currents). ECL intensity-time traces were recorded simultaneously to amperometric/voltammetric currents by using a photomultiplier tube (PMT, Hamamatsu R4632) and amplifying the signal with a Keithley Picoammeter. ECL emission was imaged with an epifluorescence microscope (Leica DMI6000) using an inverted 40x microscope objective and detected by an electron multiplying charged coupled device camera (EMCCD, Hamamatsu 9100-13.)

Results and discussion

As a first step in evaluation of coreactant ECL in nanofluidic channels, we performed cyclic voltammetry while simultaneously detecting luminescence intensity. It was recorded using a PMT as a photodetector. Figure 3 shows the current of the top Pt electrode using a solution of 10 mM $[Ru(bpy)_3]^{2+}$, 0.1 M TPA, and 0.1 M $TBAPF_6$ in acetonitrile. Onset of current and ECL in the nanochannel are as expected for a coreactant route on Pt electrode material and identical to macroscopic Pt electrodes [6]. In aqueous media, platinum might be oxidized, generating an oxide layer that prevents the efficient oxidation of TPA and thus the effective generation of ECL [25]. In the forward sweep, the onset of light emission is delayed by approximately 0.5 V compared to the onset of an oxidation current. This delay indicates a negligible contribution by the "revisited" route (Fig. 1c) [16, 17]. Indeed, as already mentioned, this pathway requires only the oxidation of the coreactant. The oxidation of deprotonated TPA produces the cation radical $TPA^{\bullet+}$ (reaction 6), which deprotonates rapidly to form the free radical $TPA^{\bullet}$ (reaction 7). This strong reductant radical reduces $[Ru(bpy)_3]^{2+}$ to $[Ru(bpy)_3]^{+}$ (reaction 10). $TPA^{\bullet+}$ oxidizes $[Ru(bpy)_3]^{+}$ to generate the excited state $[Ru(bpy)_3]^{2+*}$ (reaction 11). This mechanistic path is characterized by the facts that ECL starts simultaneously with TPA oxidation and that $[Ru(bpy)_3]^{2+}$ is not oxidized directly at the electrode surface.

Stepping the working electrode between a low and high (oxidizing) potential allows turning ECL on and off instantaneously. We recorded step-chronoamperometric traces of the same acetonitrile solution (10 mM $[Ru(bpy)_3]^{2+}$, 0.1 M TPA, and 0.1 M $TBAPF_6$) by keeping the bottom electrode potential of a nanofluidic device biased constantly at − 1.5 V and stepping the top electrode between 0 V and 2 V vs. Ag (see Fig. 4). At the − 1.5 V potential imposed to the bottom electrode, $[Ru(bpy)_3]^{2+}$ is constantly being reduced to $[Ru(bpy)_3]^{+}$. While the top electrode is kept at 0 V, no light is emitted, and a current of about 0.3 μA is generated at the top electrode by oxidation of $[Ru(bpy)_3]^{+}$ (and approximately − 0.3 μA at the bottom electrode). It means that $[Ru(bpy)_3]^{2+}$ and $[Ru(bpy)_3]^{+}$ undergo redox cycling [19] between both electrodes along the entire nanochannel. When switching the top electrode potential to 2 V, TPA and $[Ru(bpy)_3]^{2+}$ are being oxidized there. Consequently, the current increases at both electrodes. This increase as well as the anti-

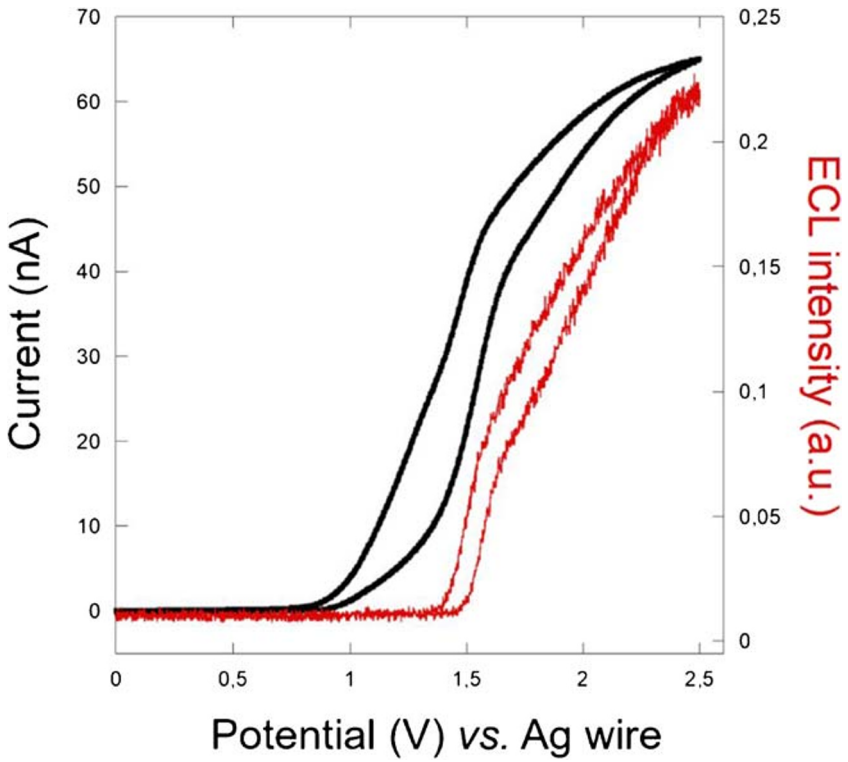

Fig. 3 Cyclic voltammogram (black curve) and corresponding ECL signal (red curve) of the top electrode in a nanofluidic device. Bottom electrode was disconnected. The acetonitrile solution contains 10 mM $[Ru(bpy)_3]^{2+}$, 0.1 M TPA, and 0.1 M $TBAPF_6$. A silver wire was used as a pseudo-reference electrode. Scan rate 0.1 V/s. Light intensity was recorded through the bottom electrode and device substrate

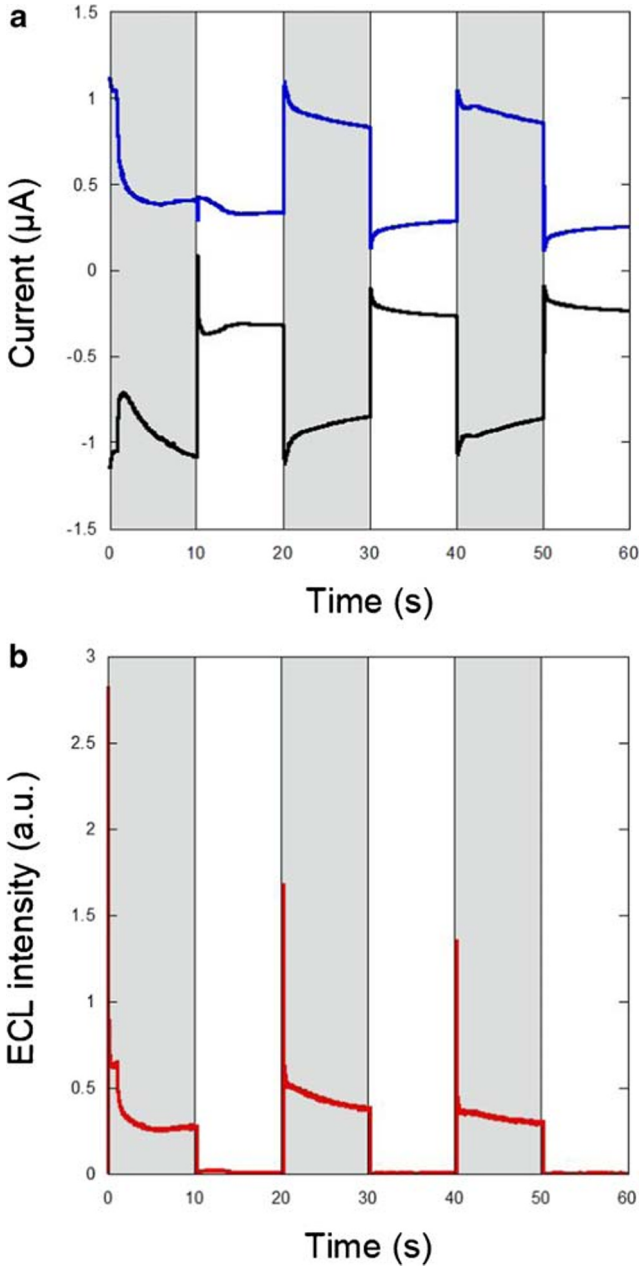

Fig. 4 **a** Chronoamperometric currents at the top (blue curve) and bottom (black curve) electrodes, and **b** corresponding ECL signals (red curve). The bottom electrode was maintained at − 1.5 V while the top electrode was pulsed for 10 s between 0 V and 2 V (highlighted in gray) vs. Ag. The acetonitrile solution contains 10 mM $[Ru(bpy)_3]^{2+}$, 0.1 M TPA, and 0.1 M $TBAPF_6$. An Ag wire was used as a pseudo-reference electrode

correlation of both current-time traces indicates an annihilation reaction (reactions 1–4). The current increases as the annihilation route is much more efficient in shuttling electrons across the inter-electrode distance compared to redox cycling [20, 26].

The ECL emission intensity reaches a steady state after a short time response and an initial spike in intensity. ECL intensity and current response are consistent with previously obtained chronoamperometric traces recorded in absence of any coreactant [20]. Thus, our results indicate that a direct current annihilation mode dominates light generation by a coreactant route. In other words, the annihilation route operates even in the presence of a 100 mM TPA coreactant concentration (but is affected by TPA as shown below). However, this experimental result does not provide us any information on the distribution of the ECL emission. For that, we recorded the ECL images of the nanofluidic channels in different conditions.

By imaging the spatial intensity profiles emitted from the nanochannel, annihilation, and coreactant ECL routes can be clearly distinguished. In Fig. 5, three different steady-state situations are compared, showing bright-field micrographs in the top row, ECL images in the center, and overlays of both in the bottom row:

Column a) Mixed annihilation/coreactant mode in the presence of TPA: a solution of 10 mM $[Ru(bpy)_3]^{2+}$, 0.1 M TPA, and 0.1 M $TBAPF_6$ in acetonitrile is used. The top and bottom electrodes are biased at 2 V and − 1.5 V, respectively, i.e., the same condition shown used in step-chronoamperometry (Fig. 4, top electrode stepped up to 2 V).

Column b) Coreactant mode: the same acetonitrile solution of 10 mM $[Ru(bpy)_3]^{2+}$, 0.1 M TPA, and 0.1 M $TBAPF_6$ reacts in a coreactant mode as oxidation takes place at the bottom electrode biased at 2 V (top electrode biased at 0 V).

Column c) Annihilation mode without TPA: a solution without TPA coreactant reacts in annihilation mode with a bias of 2 V and − 1.5 V at the top and bottom electrodes, respectively. (This biasing scheme is identical to (a), except that no TPA is added.)

In the case of mixed annihilation/coreactant ECL shown in Fig. 5a, only faint ECL emission is observed along the entire nanochannel, indicating an annihilation reaction. However, the ECL intensity is extremely low in comparison to the same conditions without TPA (Fig. 5c). As 0.1 M TPA is present, coreactant and annihilation routes compete in this biasing scheme; light emission by annihilation is observed (and likely a contribution by coreactant ECL, see below for discussion and comparison with numerical results). Light intensity is reduced considerably, which is most probably related to some side-reactions with TPA end-products [27, 28] generated by oxidation or reduction (see Electronic Supplementary Material (ESM) for a numerical approximation). The formation of end-products by $TPA^{\bullet}$ radical oxidation (reaction 12) is likely enhanced in the small nanochannel as the radicals are oxidized at the electrode surface directly after their generation. These end-products remain in the nanochannel due to slow diffusion out of this confined volume.

In coreactant mode (see Fig. 5b), ECL is generated by oxidation at a high potential of 2 V imposed at the bottom electrode in the presence of TPA. As the top electrode is biased at 0 V, $[Ru(bpy)_3]^{2+}$ cannot be reduced further there, and annihilation cannot take place. The same ECL emission

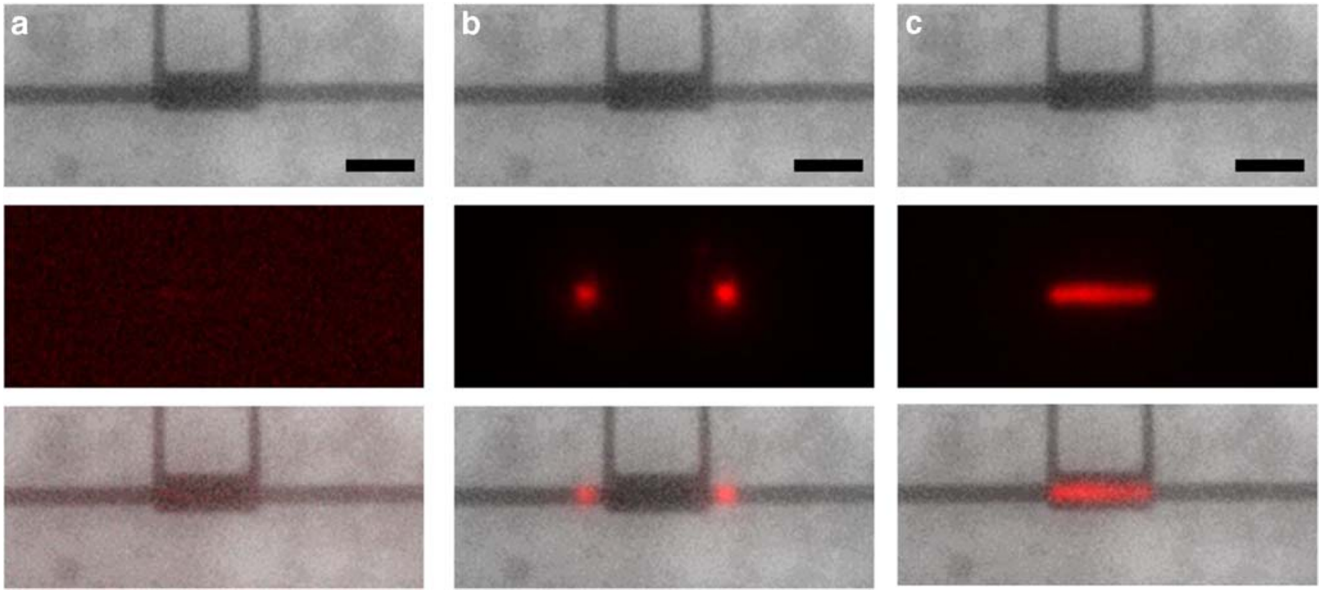

Fig. 5 From top to bottom: bright-field optical images of the nanofluidic device (scale bar: 10 μm), ECL images recorded in the dark, and overlays of both images. **a**, **b** ECL images were recorded in an acetonitrile solution containing 10 mM $[Ru(bpy)_3]^{2+}$, 0.1 M $TBAPF_6$, and 0.1 M TPA. **a** Mixed annihilation/coreactant mode in presence of TPA: the bottom and top electrodes were maintained at − 1.5 V and 2 V, respectively. **b** Coreactant mode: the bottom and top electrodes were maintained at 2 V and 0 V, respectively. **c** Same solution but without TPA. Annihilation mode without TPA: the bottom and top electrodes were maintained at − 1.5 V and 2 V, respectively. An Ag wire was used as a pseudo-reference electrode. The ECL images were coded with different ECL intensity scales

profile is obtained if the potentials are reversed between both electrodes (i.e., 0 V and 2 V for the bottom and top electrodes, respectively). In this case, light is observed exclusively at the level of the access hole areas. In any coreactant route, TPA molecules cannot be recycled, instead ending up as inactive iminium cation species [27]. As the reactions require constant replenishing of TPA, light emission is excluded from the nanochannel volume. In other words, upon stepping electrodes and initiating ECL, TPA molecules present within the channel are used up initially and converted into inactive end-product within microseconds (while we speculate above that a fraction of $TPA^{\bullet+}$ radicals could travel 100 nm across the nanochannel to be recycled, the short radical life time prohibits sustained recycling within the channel as well any significant longitudinal diffusion from the access holes into the channel). In the imaged steady state, the emission profile is determined by diffusion of TPA molecules from the bulk reservoir to the electrode area where $[Ru(bpy)_3]^{2+}$ is oxidized into $[Ru(bpy)_3]^{3+}$ and reacts with the TPA diffusing from the reservoirs. TPA cannot enter the center of the nanochannel because it is consumed by reactions 7, 8, and 10, either by reacting with the luminophore or by deprotonation at the level of the access holes. Light emission is determined by the mechanistic pathway; its profile is limited by the diffusion of the electrogenerated $[Ru(bpy)_3]^{3+}$ that reacts with TPA and by the lifetime of TPA radicals, i.e., by the short distance they can diffuse away from the electrodes located in the nanochannel. It means, that, in the coreactant mode, the diffusion of the sacrificial coreactant governs the ECL behavior of the nanofluidic channels and the location of the ECL-emitting region. ECL imaging may be essential in various configurations to resolve spatially the ECL-emitting region and to decipher complex mechanistic situations [17, 29]. For example, Francis and coworkers have been able to demonstrate that the cathodic reactions of $[Ru(bpy)_3]^{2+}$/TPA actually arise from anodic reactions at the counter electrode using ECL imaging [29]. In the reported situation, one could envision from the PMT results that ECL emission in the coreactant mode occurred in the nanochannels. This would lead to a wrong interpretation of the ECL data. However, ECL imaging experiments show clearly that it is not the case. In steady-state conditions employed here, the ECL-emitting domain is limited to the access holes. ECL imaging completes in an essential way the information obtained from PMT detection.

In annihilation mode (Fig. 5c), as reported previously [20], bright emission is emitted from the area of overlapping electrodes. Reactions 1–4 take place, and the luminophores constantly cycle between three different oxidation states as they shuttle electrons across the nanochannel and generate strong ECL. As $[Ru(bpy)_3]^{2+}$ molecules are not used up in this cycling process, and oxidized as well as reduced states return to the + 2 oxidation state during the annihilation/recombination reaction, light emission intensity is homogenous along the entire nanochannel. Both top electrode and bottom electrode participate in annihilation ECL, and, thus, no emission is observed in the access hole area, in which only the bottom electrode is exposed to the bulk solution.

In brief, ECL imaging experiments reveal two completely different situations. In the annihilation mode, ECL emission is confined in the nanochannel whereas ECL is limited to the access holes in the coreactant mode.

Different emission profiles are highlighted by linear intensity profiles evaluated at the center of the nanochannel as shown in Fig. 6 (peaks are broadened by convolution with the resolution-limited imaging optics). The blue curve, corresponding to coreactant emission (shown in Fig. 5b), shows a peak-to-peak distance of 26.7 μm in good agreement with the distance of the access holes; devices were fabricated with a nominal center-to-center distance of access holes of 26 μm. The red curve, corresponding to annihilation ECL (compare Fig. 5c), shows emission over a length of 20 μm in the area of overlapping top and bottom electrodes. The black curve depicts the profile for mixed ECL (see Fig. 5a), showing a similar profile as the annihilation curve at a strongly attenuated intensity. In this mixed mode, annihilation very likely outcompetes coreactant ECL as luminophores are very efficiently recycled at short diffusion times with a turnaround time below approximately 5 μs. The contributions of both coreactant routes on the other hand suffer from concentration polarization and depletion of TPA at the electrode area with a limiting diffusional TPA influx from the bulk.

We modeled the ECL emission profiles using two-dimensional finite element simulation (COMSOL Multiphysics, see ESM). Figure 7 shows the expected emission intensity, modeled as excited luminophore concentration $[Ru(bpy)_3]^{2+}$*, for bulk concentrations of 10 mM $[Ru(bpy)_3]^{2+}$ and 100 mM TPA. In Fig. 7a, reactants are oxidized at the top and reduced at the bottom electrode, corresponding to the mixed annihilation/coreactant pathways shown in Fig. 5a and the black curve in Fig. 6 (Eqs. 1–3, 5–8, 10, and 11 were calculated). In agreement with the experiments, light emission is confined to the channel area, and emission intensity increases at the edges of the channel, indicating competition between annihilation and coreactant pathways. Looking closely at the profile in Fig. 6, also experimentally such a slight intensity increase towards the channel ends can be observed.

In Fig. 7b, the coreactant ECL is shown with oxidation at the bottom electrode (both coreactant pathways, reaction 5–8, 10, and 11). In agreement with the experimental results (Fig. 5b), emission is confined to the access hole area. The extension of $[Ru(bpy)_3]^{2+}$* diffusion into the nanochannel is limited to < 1 μm. This is dictated and limited by the lifetime τ of the $TPA^{\bullet+}$ cation radical before deprotonation; reaction 6 has a deprotonation rate constant of $k_6 = 3500\ s^{-1}$ [16, 17, 30]. Simulations can give further insight into which coreactant pathway is dominant. A numerical evaluation of both possible coreactant mechanisms reveals that 30% of light results from $[Ru(bpy)_3]^{2+}$ oxidation by TPA, and 70% by direct oxidation at the bottom electrode (see ESM for this comparison). Figure 7c shows a $[Ru(bpy)_3]^{2+}$* concentration profile for the annihilation reaction in good agreement with the experimental results [20]. Overall, simulation results match well with light emission profiles observed in the experiments and corroborate the interpretation that different reaction and biasing scheme lead to very different intensity profiles in the confined geometry of a nanochannel.

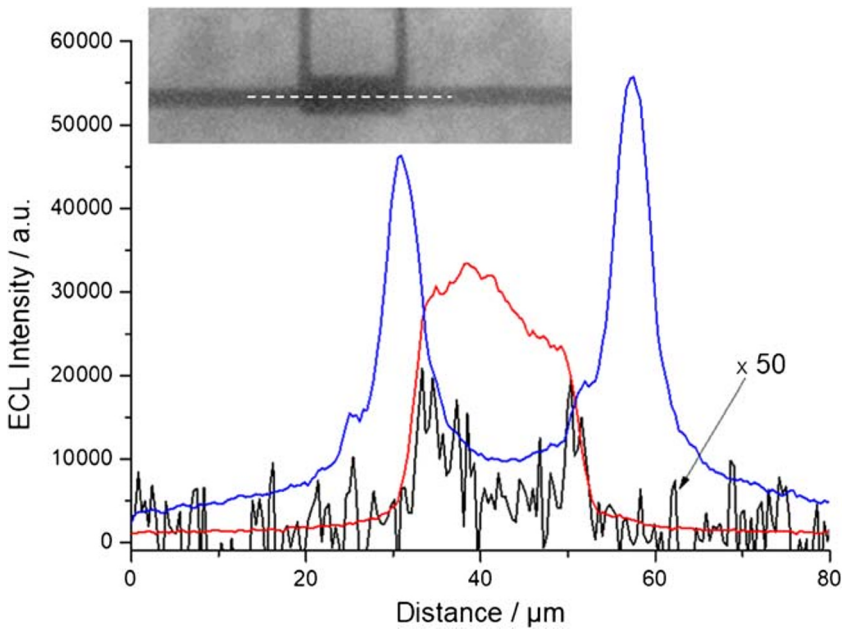

Fig. 6 ECL intensity profiles along the center of the nanochannel extracted from Fig. 5 in the coreactant mode (blue curve, corresponding to Fig. 5b), the mixed annihilation/coreactant mode with added TPA coreactant (black curve, compare Fig. 5a) and the annihilation mode without TPA (red curve, compare Fig. 5c). The insert shows the optical image of the nanochannel and the ECL intensity profiles are taken along the dashed line

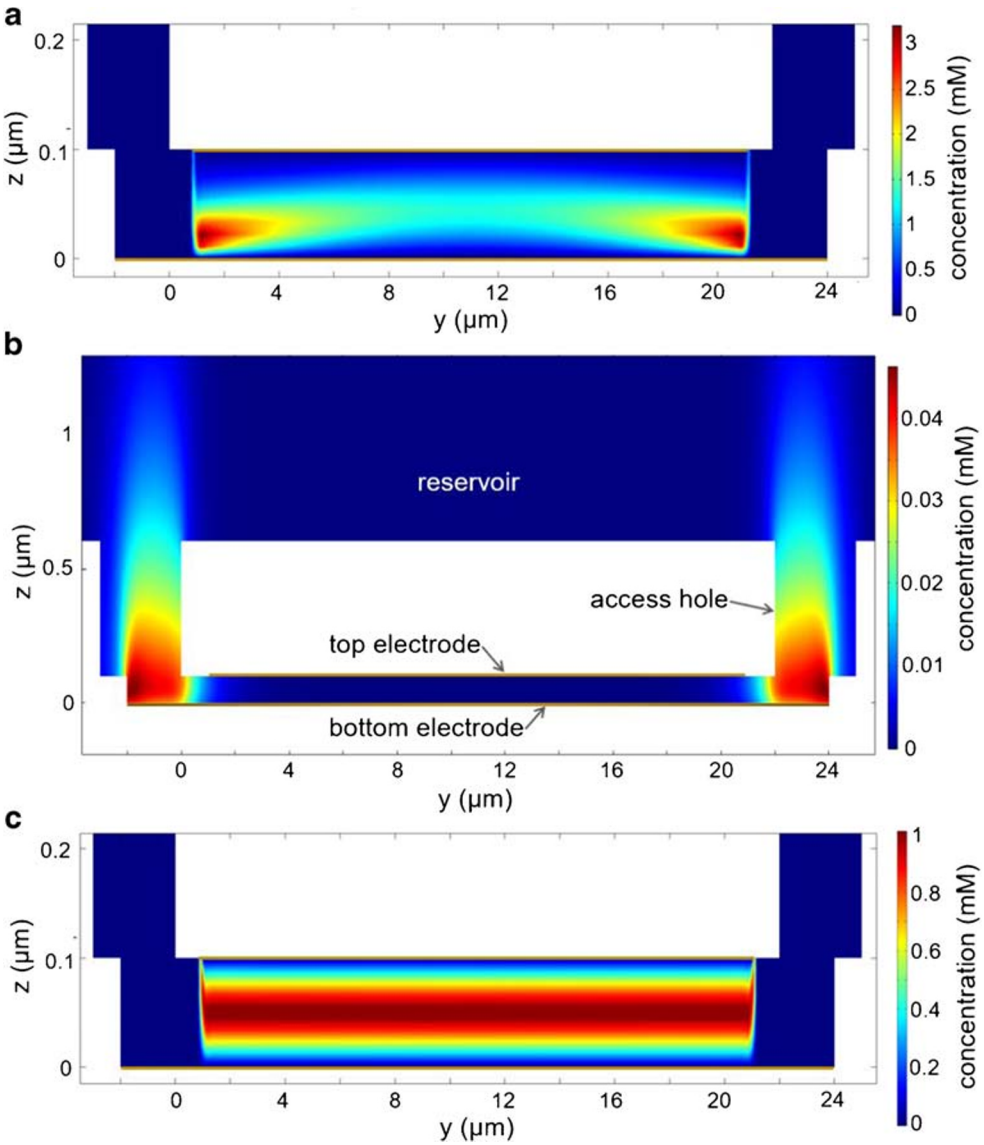

Fig. 7 Two-dimensional finite element simulation of a cross section of a nanofluidic device. The concentration of $[Ru(bpy)_3]^{2+*}$ is shown, which is equivalent to intensity profiles of light emission. **a** Mixed coreactant/annihilation reactions with oxidation at the top and reduction at the bottom electrode. **b** Coreactant pathway with oxidation of $[Ru(bpy)_3]^{2+}$ and TPA taking place at the bottom electrode (the top electrode is inactive). **c** Annihilation pathway. Bulk reservoir concentrations of 10 mM $[Ru(bpy)_3]^{2+}$ and 100 mM TPA were used for the calculations shown in **a** and **b**, and exclusively 10 mM $[Ru(bpy)_3]^{2+}$ was used for **c**. Note the skewed aspect ratios of 10:1 in panels **a** and **c** and 40:10 in **b**. Panels **a**, **b**, **c** directly correspond to the experimental profiles shown in Figs. 5 and 6

Conclusion

We investigated coreactant electrochemiluminescence in nanoscale confinement for the first time. Our results reveal that spatial light emission profiles are determined by access of the coreactant to the electrode surface. As the TPA coreactant concentration is instantaneously depleted in the nanochannel upon biasing the electrodes, light emission is excluded from this strongly confined volume. This observation is in a strong contrast to annihilation ECL in which luminophores are constantly and efficiently recycled in between both electrodes, leading to bright and homogenous light emission along the entire nanochannel volume. We further demonstrate that steady-state imaging of ECL (as opposed to measuring intensity) is an essential tool for determining mechanistic pathways of ECL light generation. When accompanied by complementary finite element simulation, imaging yields additional insight into the exact contribution of different pathways in the case of mixed ECL, in which coreactant and annihilation pathways compete. Annihilation ECL of $[Ru(bpy)_3]^{2+}$ does not work well in aqueous solutions due to the required low reduction bias lying outside of the potential window of typical electrode materials. Coreactant ECL, on the other hand, is extensively used in biosensing applications such as in immunoassays. Our results will form the basis for future experiments of enhanced ECL biosensing in nanoscale confinement.

Compliance with ethical standards

This article does not contain any studies with human or animal subjects performed by any of the contributing authors.

Conflict of interest The authors declare that they have no conflict of interest.

References

1. Bard AJ. Electrogenerated chemiluminescence. New-York: M. Dekker; 2004.
2. Sojic N, editor. Analytical electrogenerated chemiluminescence: from fundamentals to bioassays. Detection Science: Royal Society of Chemistry (RSC) Publishing; 2020.
3. Forster RJ, Bertoncello P, Keyes TE. Electrogenerated chemiluminescence. Annual Rev Anal Chem. 2009;2(1):359–85. https://doi.org/10.1146/annurev-anchem-060908-155305.
4. Liu Z, Qi W, Xu G. Recent advances in electrochemiluminescence. Chem Soc Rev. 2015;44(10):3117–42. https://doi.org/10.1039/c5cs00086f.
5. Richter MM. Electrochemiluminescence (ECL). Chem Rev. 2004;104(6):3003–36. https://doi.org/10.1021/cr020373d.
6. Miao W. Electrogenerated chemiluminescence and its biorelated applications. Chem Rev. 2008;108(7):2506–53. https://doi.org/10.1021/cr068083a.
7. Sojic N, Arbault S, Bouffier L, Kuhn A. Applications of electrogenerated chemiluminescence in analytical chemistry. In: Miomandre F, Audebert P, editors. Luminescence in electrochemistry: applications in analytical chemistry. Cham: Physics and Biology. Springer International Publishing; 2017. p. 257–91. https://doi.org/10.1007/978-3-319-49137-0_8.
8. Valenti G, Rampazzo E, Kesarkar S, Genovese D, Fiorani A, Zanut A, et al. Electrogenerated chemiluminescence from metal complexes-based nanoparticles for highly sensitive sensors applications. Coord Chem Rev. 2018;367:65–81. https://doi.org/10.1016/j.ccr.2018.04.011.
9. Zhai Y, Zhu Z, Zhou S, Zhu C, Dong S. Recent advances in spectroelectrochemistry. Nanoscale. 2018;10(7):3089–111. https://doi.org/10.1039/c7nr07803j.
10. Garoz-Ruiz J, Perales-Rondon JV, Heras A, Colina A. Spectroelectrochemical sensing: current trends and challenges. Electroanalysis. 2019;31(7):1254–78. https://doi.org/10.1002/elan.201900075.
11. Lozeman JJA, Führer P, Olthuis W, Odijk M. Spectroelectrochemistry, the future of visualizing electrode processes by hyphenating electrochemistry with spectroscopic techniques. Analyst. 2020. https://doi.org/10.1039/c9an02105a.
12. Kapturkiewicz A. Electrochemical generation of excited intramolecular charge-transfer states. ChemElectroChem. 2017;4(7):1604–38. https://doi.org/10.1002/celc.201600865.
13. Amatore C, Pebay C, Servant L, Sojic N, Szunerits S, Thouin L. Mapping electrochemiluminescence as generated at double-band microelectrodes by confocal microscopy under steady state. ChemPhysChem. 2006;7:1322–7.
14. Doeven EH, Zammit EM, Barbante GJ, Hogan CF, Barnett NW, Francis PS. Selective excitation of concomitant electrochemiluminophores: tuning emission color by electrode potential. Angew Chem Int Ed. 2012;51(18):4354–7. https://doi.org/10.1002/anie.201200814.
15. Liu X, Shi L, Niu W, Li H, Xu G. Environmentally friendly and highly sensitive ruthenium(II) Tris(2,2′-bipyridyl) electrochemiluminescent system using 2-(dibutylamino)ethanol as co-reactant. Angew Chem Int Ed. 2007;46(3):421–4. https://doi.org/10.1002/anie.200603491.
16. Miao W, Choi J-P, Bard AJ. Electrogenerated chemiluminescence 69: the Tris(2,2′-bipyridine)ruthenium(II), (Ru(bpy)32+)/Tri-n-propylamine (TPrA) system eevisited a new route involving TPrA•+ cation radicals. J Am Chem Soc. 2002;124(48):14478–85. https://doi.org/10.1021/ja027532v.
17. Sentic M, Milutinovic M, Kanoufi F, Manojlovic D, Arbault S, Sojic N. Mapping electrogenerated chemiluminescence reactivity in space: mechanistic insight into model systems used in immunoassays. Chem Sci. 2014;5(6):2568–72. https://doi.org/10.1039/c4sc00312h.
18. Rinklin P, Mayer D, Wolfrum B. Electrochemical nanocavity devices. In: Schöning MJ, Poghossian A, editors. Label-free biosensing: advanced materials. Cham: Devices and Applications. Springer International Publishing; 2018. p. 199–214. https://doi.org/10.1007/5346_2017_8.
19. White HS, McKelvey K. Redox cycling in nanogap electrochemical cells. Curr Op Electrochem. 2018;7:48–53. https://doi.org/10.1016/j.coelec.2017.10.021.
20. Al-Kutubi H, Voci S, Rassaei L, Sojic N, Mathwig K. Enhanced annihilation electrochemiluminescence by nanofluidic confinement. Chem Sci. 2018;9(48):8946–50. https://doi.org/10.1039/c8sc03209b.
21. Cui J, Mathwig K, Mampallil D, Lemay SG. Potential-controlled adsorption, separation, and detection of redox species in nanofluidic devices. Anal Chem. 2018;90(12):7127–30. https://doi.org/10.1021/acs.analchem.8b01719.
22. Kang S, Nieuwenhuis AF, Mathwig K, Mampallil D, Kostiuchenko ZA, Lemay SG. Single-molecule electrochemistry in nanochannels: probing the time of first passage. Farad Discuss. 2016;193(0):41–50. https://doi.org/10.1039/c6fd00075d.
23. Krause KJ, Mathwig K, Wolfrum B, Lemay SG. Brownian motion in electrochemical nanodevices. Eur Phys J SpecTop. 2014;223(14):3165–78. https://doi.org/10.1140/epjst/e2014-02325-5.
24. Mathwig K, Lemay SG. Pushing the limits of electrical detection of ultralow flows in nanofluidic channels. Micromachines. 2013;4(2):138–48.
25. Valenti G, Fiorani A, Li H, Sojic N, Paolucci F. Essential role of electrode materials in electrochemiluminescence applications. ChemElectroChem. 2016;3(12):1990–7. https://doi.org/10.1002/celc.201600602.
26. Mathwig K, Sojic N. Towards determining kinetics of annihilation electrogenerated chemiluminescence by concentration-dependent luminescent intensity. J Anal Test. 2019;3(2):160–5. https://doi.org/10.1007/s41664-019-00094-z.
27. Qiu R, Zhang X, Luo H, Shao Y. Mass spectrometric snapshots for electrochemical reactions. Chem Sci. 2016;7(11):6684–8. https://doi.org/10.1039/c6sc01978a.
28. Qin X, Gu C, Wang M, Dong Y, Nie X, Li M, et al. Triethanolamine-modified gold nanoparticles synthesized by a one-pot method and their application in electrochemiluminescent immunoassay. Anal Chem. 2018;90(4):2826–32. https://doi.org/10.1021/acs.analchem.7b04952.
29. Theakstone AG, Doeven EH, Conlan XA, Dennany L, Francis PS. 'Cathodic' electrochemiluminescence of [Ru(bpy)3]2+ and tri-n-propylamine confirmed as emission at the counter electrode. Chem Commun. 2019;55(49):7081–4. https://doi.org/10.1039/c9cc03201k.
30. Valenti G, Scarabino S, Goudeau B, Lesch A, Jović M, Villani E, et al. Single cell electrochemiluminescence imaging: from the proof-of-concept to disposable device-based analysis. J Am Chem Soc. 2017;139(46):16830–7. https://doi.org/10.1021/jacs.7b09260.

Analytical and Bioanalytical Chemistry

Electronic Supplementary Material

Electrochemiluminescence reaction pathways in nanofluidic devices

Silvia Voci, Hanan Al-Kutubi, Liza Rassaei, Klaus Mathwig, Neso Sojic

1. Finite element calculations

We employed COMSOL Multiphysics 5.2a for two-dimensional finite element calculations of steady-state concentration profiles in a nanochannel based on our previous simulations [1, 2]. The geometry consists of a 26 µm long and 100 nm high nanochannel. This channel is coupled via two 3 µm wide and 500 nm high access channels to a 48 µm by 7 µm reservoir (see Figure 7 in the main text). The boundaries of the reservoirs are set at constant concentrations of 100 mM TPA and 10 mM $[Ru(bpy)_3]^{2+}$.

Molecules in solution move exclusively by diffusion. Thus, mass transport for all species *j* is governed by Fick's law $\frac{\partial c_j}{\partial t} = D_j \nabla^2 c_j$. We set all diffusion coefficients D_j to 10^{-9} $m^2 s^{-1}$.

For co-reactant pathways, we adapted the numerical reaction model of Valenti et al. [3]. In this pathway, $[Ru(bpy)_3]^{2+}$ and TPA are oxidized at an electrode surface. The following reactions occur:

$$[Ru(bpy)_3]^{2+} \xrightarrow{k_1} [Ru(bpy)_3]^{3+} + e^- \quad \text{(S1)}$$

$$TPA \xrightarrow{k_2} TPA^{\bullet+} + e^- \quad \text{(S2)}$$

$$TPA^{\bullet} \xrightarrow{k_3} P1 + e^- \quad \text{(S3)}$$

Here, k_1 is the rate constant for $[Ru(bpy)_3]^{2+}$ oxidation with

$$k_1 = k_0 \exp\left[\frac{(1-\alpha)F(E_{bot}-E_h)}{RT}\right] \quad \text{(S4)}$$

(k_0 = 0.01 m s^{-1} standard rate constant, α = 0.5 charge transfer coefficient, *F*: Faraday constant, *R*: gas constant, *T*: temperature, E_{bot} = 1.5 V electrode potential, E_h: formal potential for $[Ru(bpy)_3]^{2+}$ oxidation). TPA is oxidized in the same way with the rate constant $k_2 = k_0 \exp\left[\frac{(1-\alpha)F(E_{bot}-E_0)}{RT}\right]$ (E_0: formal potential for TPA oxidation). The radical $TPA^{\bullet}$ reacts also very fast to the product P1 with $k_3 = k_0 \exp\left[\frac{(1-\alpha)F(E_{bot}-E_{0d})}{RT}\right]$ (E_{0d}: formal potential for TPA oxidation). All these oxidation reactions at the electrode are fast at the chosen potential and do not limit the overall rate kinetics and concentration distributions.

In the bulk solution in the nanochannel, access holes and reservoirs, two reactions involving TPA compounds are competing. In a first reaction, the 'revisited' route, $TPA^{\bullet}$ radicals and $TPA^{\bullet+}$cation radicals react with $[Ru(bpy)_3]^{2+}$ to form the excited luminophores:

$$TPA^{\bullet} + TPA^{\bullet+} + [Ru(bpy)_3]^{2+} \xrightarrow{k_5} P1 + TPA + [Ru(bpy)_3]^{2+*} \quad \text{(S5)}$$

with $k_5 = 10^6$ M^{-1} s^{-1}.

Simultaneously, $TPA^{\bullet+}$ cation radicals formed at the electrodes deprotonate

$$TPA^{\bullet+} \xrightarrow{k_6} TPA^{\bullet} + H^+ \quad \text{(S6)}$$

with the deprotonation rate constant k_6 = 3500 s^{-1}.

Excited luminophores return to the ground state $[Ru(bpy)_3]^{2+}$ by emitting light

$$[Ru(bpy)_3]^{2+*} \xrightarrow{k_{em}} [Ru(bpy)_3]^{2+} + h\nu \quad \text{(S7)}$$

with a high emission rate of k_{em} = 10^8 s^{-1}. (We did not consider a light profile hν explicitly and use the equivalent $[Ru(bpy)_3]^{2+*}$ profile instead.)

The light emission profile is predominantly governed by the deprotonation rate k_6. This rate is identical to the lifetime of $TPA^{\bullet+}$; it determines how far these radical cations can diffuse away from the electrode before deprotonation. It means that this lifetime sets a limit to the maximal distance from the electrode surface at which light can be emitted.

An alternative pathway for the formation of excited states, and, thus, light emission, is the reduction of $[Ru(bpy)_3]^{3+}$ by $TPA^{\bullet}$ radicals:

$$TPA^{\bullet} + [Ru(bpy)_3]^{3+} \overset{k_5}{\rightarrow} P1 + [Ru(bpy)_3]^{2+*} \quad \text{(S8)}$$

In the annihilation pathway, additional reactions take place, luminophores are reduced at the cathode:

$$[Ru(bpy)_3]^{2+} + e^- \overset{k_1}{\rightarrow} [Ru(bpy)_3]^{1+}, \quad \text{(S9)}$$

and recombination/annihilation of reduced and oxidized luminophores ($[Ru(bpy)_3]^{+}$ and $[Ru(bpy)_3]^{3+}$, respectively) takes place in the bulk of the nanochannel generating the excited $[Ru(bpy)_3]^{2+*}$ state:

$$[Ru(bpy)_3]^{+} + [Ru(bpy)_3]^{3+} \overset{k_{ann}}{\longrightarrow} [Ru(bpy)_3]^{2+} + [Ru(bpy)_3]^{2+*} \quad \text{(S10)}$$

Here, k_{ann} is the annihilation rate constant with a value of 10^9 M^{-1} s^{-1}. The numerical calculation also considers possible 2-electron processes of luminophore as well as consumption of excited luminophores at the electrode surface (see ref. [1,2]).

Fig. S1 show concentration profiles of all involved compounds for three pathways show in the main text (see Figure 5, 6, 7). The second row in Figure S1 is identical to Figure 7 in the main text. The numerical results show, that, in coreactant modes, the light emission profile is determined by the profile of the TPA coreactant radical, i.e., by the lifetime of $TPA^{\bullet+}$ before deprotonation.

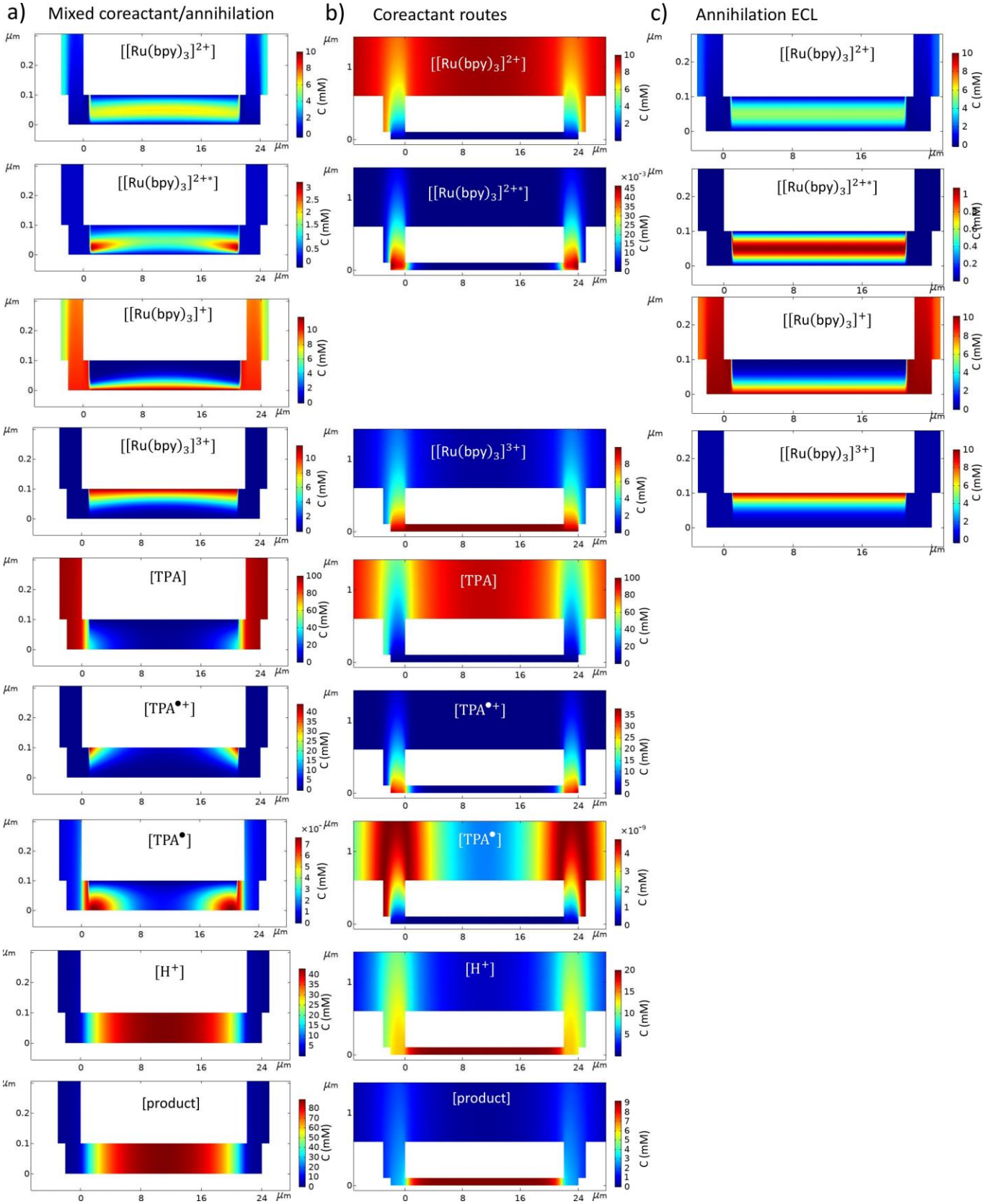

Fig. S1 Finite element calculation of excited concentration profiles for all considers compounds. Column a) Mixed coreactant/annihilation with oxidation at the top electrode and reduction at the bottom electrode. b) Both coreactant pathways with oxidation at the bottom electrode. c) Annihilation pathway with oxidation at the top and reduction at the bottom electrode. Boundary conditions are a concentration of 10 mM $[Ru(bpy)_3]^{2+}$ for all panels and additionally 100 mM TPA for a), b). Aspect rations are a) 40:1, b) 10:1; c) 40:1

2. Contributions of pathways to coreactant ECL

In coreactant ECL mode, two pathways lead to the generation of excited luminophore (see Figure 1b,c in the main text). We simulated the individual pathways separately to estimate the contribution of each reaction scheme to light generation.

In Fig. S2, $[Ru(bpy)_3]^{2+*}$ concentration profiles generated by reaction (S5) and reaction (S8) are compared. Using only eq. (S5), light is emitted at a farther distance from the oxidizing bottom electrode. No light is emitted directly at the electrode surface as $[Ru(bpy)_3]^{2+}$ is depleted there. Overall, the maximal $[Ru(bpy)_3]^{2+*}$ concentration is almost seven times lower for reaction (S5) compared to reaction (S8), i.e., light emission intensity is faint. When comparing Figures S2 b) and c), the maximal $[Ru(bpy)_3]^{2+*}$ for reaction (8) is about 80% of the concentration for the case of both pathways occur simultaneously. Therefore, we conclude, that about 80% of the light is generated via reaction (S8) and 20% via reaction (S5). Direct oxidation of $[Ru(bpy)_3]^{2+}$ dominates over the 'revisited' route.

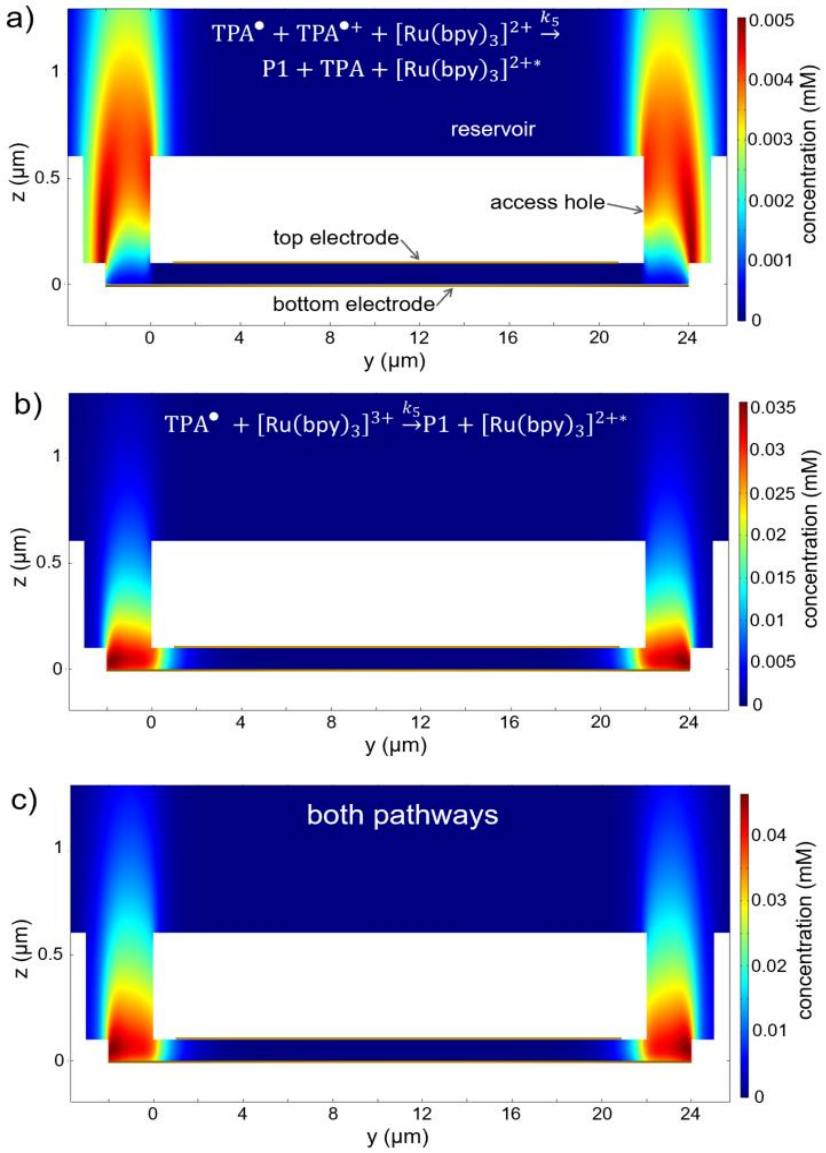

Fig. S2 Finite element calculation of excited luminophore $[Ru(bpy)_3]^{2+*}$ concentrations. Concentration profiles generated via equation (S5) and (S8) are compared in panels (a) and (b), respectively. Panel (c) shows the calculated profiles for both reactions occurring simultaneously. Note the different concentration scales, the maximal $[Ru(bpy)_3]^{2+*}$ concentration is increased 9 times for both reactions compared to eq. (S5) (The aspect ratio is skewed 10:1, panel c is identical to Figure 7b in the main text.)

3. Side reaction in mixed annihilation/coreactant ECL

The experimentally observed emission intensity of the mixed annihilation/coreactant pathway is very faint (see Figure 5a in the main text). In contrast, numerical simulations yield a very high intensity of the pathway, higher than for the individual coreactant as well as annihilation schemes (see Figures 7, S1). We suspect that possible competing side reactions involving TPA could greatly diminish the efficiency of generating exciting luminophores. Moreover, in the mixed pathway, a high concentration of inactive TPA is generated in the nanochannel where it accumulates because diffusion out of a long channel is slow (Figure S1a, bottom row, shows a high 80 mM concentration of accumulated product).

We estimate the effect of parasitic side reactions in a simulation by slightly reducing the conversion efficiency of the TPA reaction (S5) of the 'revisited' pathway by 0.1% and 1%, respectively. (Reaction S5 corresponds to equations (10, 11) in the main text). This means, in the generation of TPA and $[Ru(bpy)_3]^{2+*}$, the molarities of these products (as compared to molarities of the reaction educts) are reduced to 99.9% and 99%, respectively (compared to 100% conversion yield in all previous simulations). In other words, the concentration of TPA and $[Ru(bpy)_3]^{2+*}$ (generated by reaction S5) are both multiplied with factors 0.999 and 0.99, respectively, to simulate loss of TPA and $[Ru(bpy)_3]^{2+*}$ due to competing side reactions. In Fig. S3, $[Ru(bpy)_3]^{2+*}$ concentrations profiles are compared, showing a considerably reduced concentrations corresponding to reduced light emission with increasingly inefficient conversion.

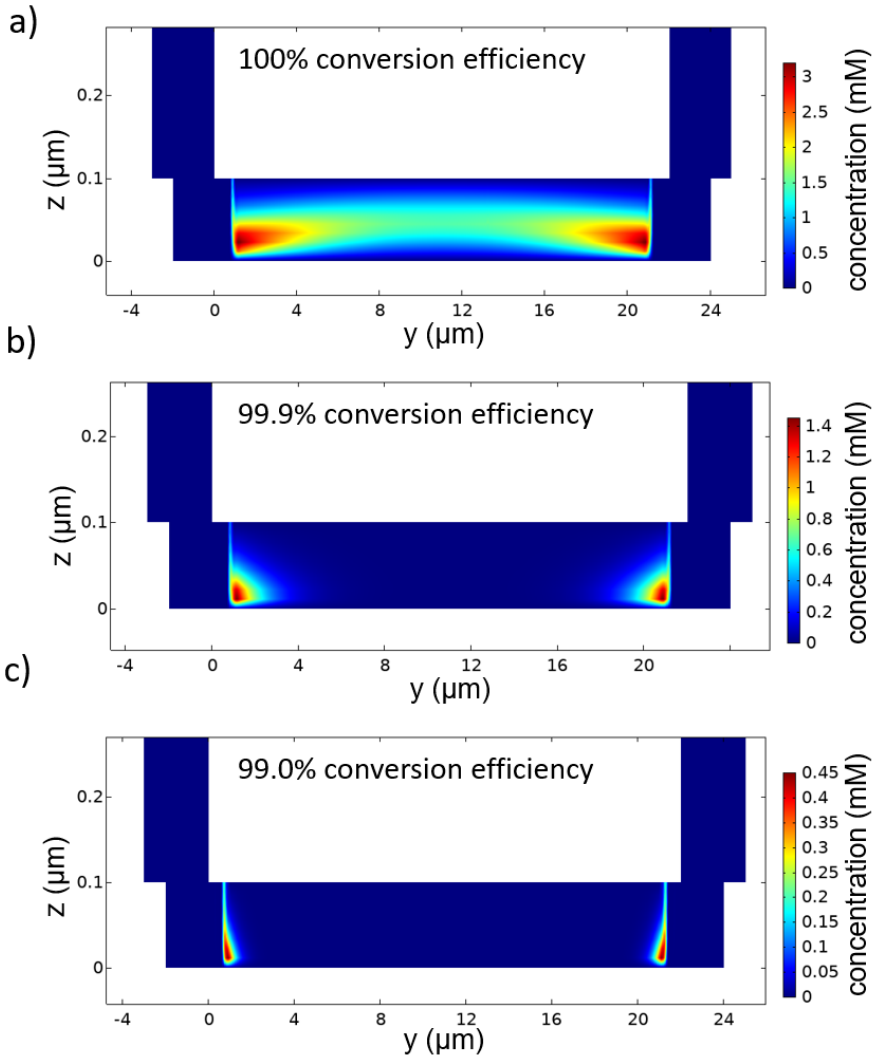

Fig. S3 Finite element calculation of excited luminophore $[Ru(bpy)_3]^{2+*}$ concentrations in a mixed coreactant/annihilation path-way. a) is identical to Figure 7a in the main text. In b) the efficiency of generating TPA and $[Ru(bpy)_3]^{2+*}$ according to reaction (S5) is reduced to 99.9%, in c) it is reduced to 99%. Note the concentration scales: $[Ru(bpy)_3]^{2+*}$ concentration is strongly reduced for reduced conversion rates

References

1. Al-Kutubi, H., Voci, S., Rassaei, L., Sojic, N., Mathwig, K.: Enhanced annihilation electrochemiluminescence by nanofluidic confinement. Chem. Sci. 9, 8946–8950 (2018). doi:10.1039/C8SC03209B
2. Mathwig, K., Sojic, N.: Towards Determining Kinetics of Annihilation Electrogenerated Chemiluminescence by Concentration-Dependent Luminescent Intensity. J. Anal. Test. (2019). doi:10.1007/s41664-019-00094-z
3. Valenti, G., Scarabino, S., Goudeau, B., Lesch, A., Jović, M., Villani, E., Sentic, M., Rapino, S., Arbault, S., Paolucci, F., Sojic, N.: Single Cell Electrochemiluminescence Imaging: From the Proof-of-Concept to Disposable Device-Based Analysis. J. Am. Chem. Soc. 139, 16830–16837 (2017). doi:10.1021/jacs.7b09260